Low-Dimensional FeS$_2$ Nanostructures for use as Hydrogen Evolution Electrocatalysts

By

Daniel J. Jasion

Submitted to the graduate degree program in Chemistry and the Graduate Faculty of the University of Kansas in partial fulfillment of the requirements for the degree of Master of Arts.

_____

Shenqiang Ren, PhD, Assistant Professor (Chair)

_____

Kevin C. Leonard, PhD, Assistant Professor

_____

Ward Thompson, PhD, Professor

Date Defended: 7 May 2015

The Thesis Committee for Daniel J. Jasion

certifies that this is the approved version of the following thesis:

Low-Dimensional FeS$_2$ Nanostructures for use as Hydrogen Evolution Electrocatalysts

_____

Shenqiang Ren, PhD, Assistant Professor (Chair)

Date approved: 7 May 2015

Abstract

The water splitting hydrogen evolution reaction which is used as an alternative method of hydrogen production currently relies on platinum group metal electrocatalysts to function. Currently this method accounts for only a small portion of actual hydrogen production. To achieve broad utilization of this method of hydrogen generation it would be beneficial if these precious metal catalysts were replaced with low-cost materials that use easily scalable production methods. Many different materials have been investigated attempting to identify effective replacements for precious metal electrocatalysts and FeS_2 nanomaterials are a class of materials that meet these utilization requirements and have a demonstrated catalytic ability. This work examines the synthetic parameters and fundamental reaction mechanism involved in the formation of novel low dimensional iron disulfide nanostructures and subsequently details their development as replacement electrocatalysts.

The low-dimensional hyperthin FeS_2 nanostructures were generated by a scalable modified hot-injection technique. Maintaining low reaction temperatures kinetically confined the reaction to its early stages. Subsequent manipulation of the sulfur in the reaction allowed for the formation of novel one (1D) and two (2D) dimensional nanostructures which were observed in both transmission electron microscopy (TEM) and scanning electron microscopy (SEM). Furthermore, increased dwell times allowed for stoichiometric control of products to produce a 1:2 Fe:S structure as characterized by energy dispersive X-ray (EDS), X-ray diffraction (XRD), and Raman spectroscopy. Additionally, these nanomaterials did not adhere to the normally observed reaction pathway and formed without undergoing growth through Ostwald ripening or orientated attachment.

Electrocatalytic performance of 1D and 2D FeS_2 materials coated on a glassy carbon electrode was tested against platinum as well as a common 3D FeS_2 structure in a phosphate

buffered solution (PBS) at neutral pH using linear sweep voltammetry (LSV). The near zero onset potential of the 2D structures was similar to platinum and both had calculated charge transfer coefficients of 0.71. Exchange current densities calculated using Butler-Volmer equations from best-fit lines yielding 2.2 and 8.0 µA cm^{-2} for the 2D structures and platinum, respectively. Scanning electrochemical microscopy (SECM) confirmed the formation of hydrogen and subsequent stability test showed stable performance for over 125 hours demonstrating that functional low-dimensional FeS$_2$ nanomaterials are promising platinum electrocatalyst replacement.

Acknowledgements

I would like to thank everyone that made this scientific endeavor possible through advice, support, and encouragement – most importantly my wife and family, Dr. Ren, our collaborators Dr. Kevin Leonard and Joe Barforoush, fellow and former graduate students Jess, Alec, and Phil, those who provided help with instrumentation Heather Shinogle, Victor Day, Travis Witte, the KU Chemistry department, and all those that provided financial support.

Table of Contents

List of Figures

List of Equations

1   Introduction

Green energy initiatives have given rise to extensive research investigating various renewable and sustainable resources. Resource diversification is desired since the goal is to shift the current reliance on fossil fuels towards renewable and sustainable materials. One such method of resource diversification revolves around the use of a renewable energy source such as solar or wind power to drive water splitting reactions and generate hydrogen.[1] This hydrogen can be used to temporarily store energy as an alternative to conventional batteries.[2] The hydrogen can also be utilized as feedstock in numerous other reactions such as the Haber process for ammonia formation.[3] However, hydrogen evolution reactions (HER) are governed by electrocatalysts which usually are comprised of a platinum group precious metal (e.g. Pt, Ir, Ru). These metals are efficient but are also incredibly costly, rare, and production can be easily thwarted when impurities are present.[4] This has led to the search for replacement materials for these catalysts that hope to achieve similar catalytic efficiencies but with reduced cost.[5] FeS_2 materials have been subject to extensive study in the context of green energy applications[6] because of the abundance of its elemental components, lack of heavy/precious metals, and low-cost.

1.1   Goals

It is the goal of this work to develop low-cost abundant FeS_2 nanomaterials that function as replacement HER electrocatalysts possessing comparable efficiency and stability to current precious metal catalysts. The focus will be on the design of large surface area to volume FeS_2 materials, in our case one dimensional (1D) and two-dimensional (2D) nanostructures, to maximize available catalytic area as well as development of stoichiometric control to form more stable FeS_2 phases instead of other less stable $Fe_{1-x}S$ stoichiometries. Furthermore, this work will address the deviant growth patterns of these low dimensional materials by presenting a new

1

set of reaction pathways and how they fit into accepted growth models. Finally a comparison of the electrocatalytic performance of 1D and 2D structures will be made in relation the standard platinum catalyst material.

1.2   The FeS$_2$ Nanoparticle Growth Model

A brief description of general nanoparticle synthetic procedures and the associated growth mechanisms must be presented to better understand the rationale behind the synthetic conditions used. It will also act as a reference for the later discussion of the low-dimensional nanoparticle growth and how this growth fits in this standard reaction pathway.
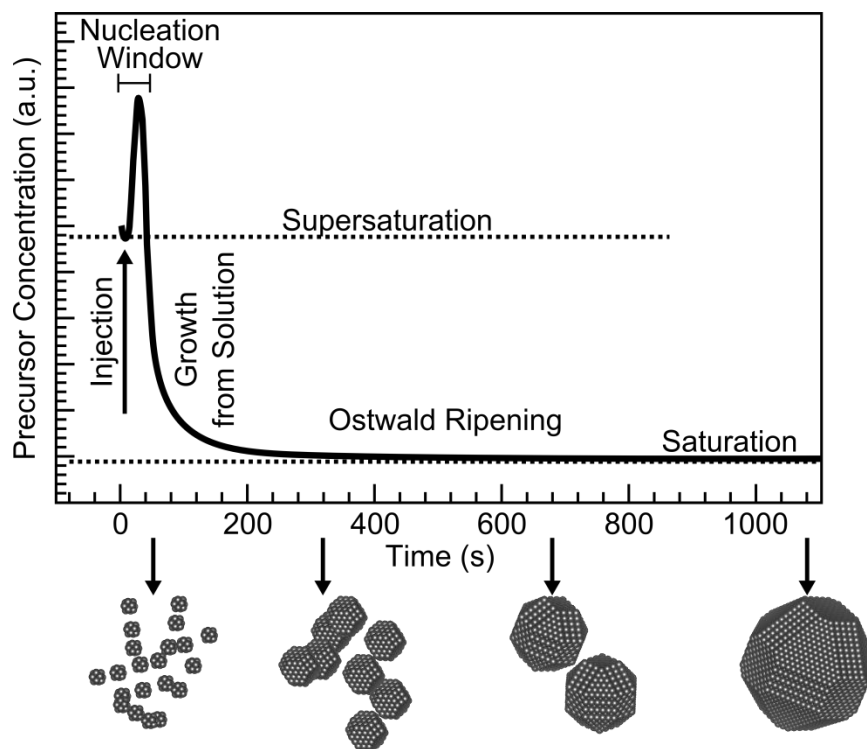
Figure 1. Stages of nucleation and growth of colloidal nanocrystals following La Mer theory. The dotted lines depict the nucleation threshold (top) and the precursor saturation limit (bottom). The effects of Ostwald ripening are pictorially presented below the plot. Adapted with permission from reference [7]

Initial nucleation and seed particle formation can be generally described by La Mer theory.[8] As described in Fig. 1 nucleation occurs to reduce the supersaturation of precursor in solution producing small seed particles and nucleation continues to occur until precursor

2

concentration falls below supersaturation levels. Precursor solutions were injected into the

reaction flask causing the initial increase in precursor concentration to supersaturation levels.

Once the nucleation stops, further size increases of these seed particles occurs by diffusion

limited growth which can be described by Ostwald ripening. In this phase of the reaction small

particles eliminate high surface energy. In essence large particles become larger and small

particles become smaller. This growth mechanism persists until monomer concentration drops

below saturation levels. This progression of nucleation through diffusion limited growth

describes most nanoparticles systems, however, it has been shown that FeS_2 systems can develop

larger structural formations of various shapes through an oriented attachment (OA) growth

mechanism.[9]
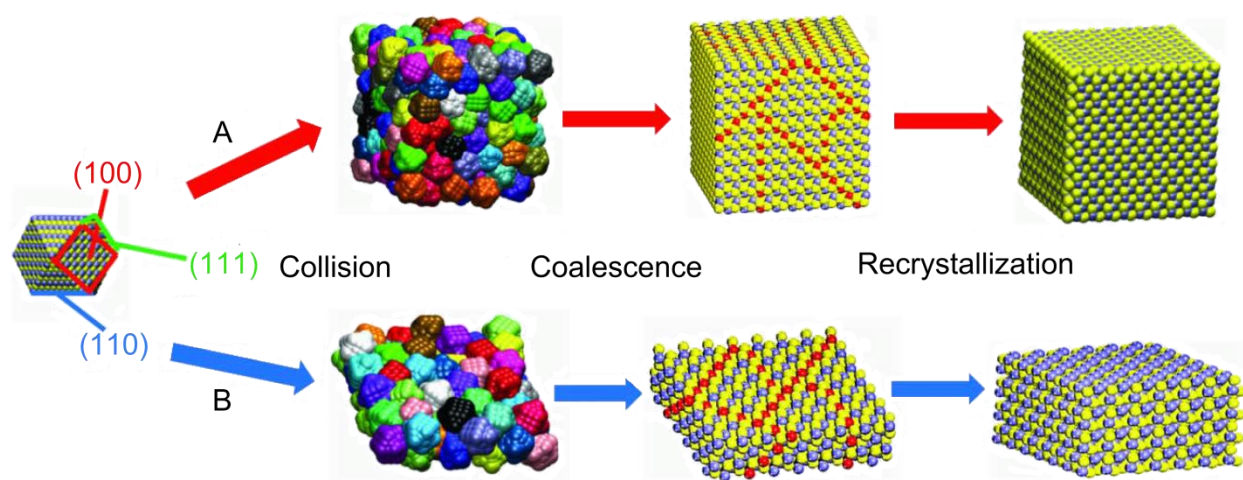
Figure 2. Oriented attachment growth mechanism in FeS_2 systems illustrating aggregation, collision, coalescence, and recrystallization steps. Adapted with permission from Reference [9]

The OA mechanism in FeS_2 systems can be broken down into four parts: (1) the

aggregation, (2) reorientation/collisions, (3) elimination/coalescence, and (4) recrystallization.

In the aggregation step small particles are brought together by various interaction forces. Once

these particles are in close proximity they reorient themselves to align and collide high energy

faces. As these faces coalesce together the coordinating ligand is expelled from the interior of

the forming structure. Finally recrystallization occurs with interparticle bond formation

3

alleviating and/or removing internal dislocations to form large nanocrystals.

Overall, this pathway from nucleation to OA outlines the fundamental growth process of standard formations of FeS_2 structures such as plates, spheres, cubes and as mentioned earlier will be used as the basis for our subsequent FeS_2 nanoparticle synthesis.

2   FeS$_2$ Nanoparticle Synthesis

2.1   Motivation

FeS_2 materials have been subject to extensive study in the context of green energy applications because of the abundance of its elemental components with iron being the fourth most abundant element in the earth's crust and sulfur is a refinery byproduct, the lack of heavy/precious metals and low-cost.[10,11] Inherent material properties found in nanoscale FeS_2 particles have led to the development of several synthetic pathways to yield a variety of nanostructures.[12-14] For catalytic work, structures that have high surface area to volume ratios (low-dimensional) are preferred; but, these atomic layer thickness low dimensional FeS_2 nanostructures have scarcely been reported. Moreover, many of the low dimensional structures that have been reported were seen as short-lived intermediate phases that lacked ideal stoichiometry (i.e. not FeS_2) and consequently not thoroughly studied.[15,16] Existing methods for producing thin low dimensional materials have utilized various deposition techniques that usually requiring additional high temperature sulfurization, or a brute force approach through cleavage.[17-19] The problem with these aforementioned methods are that they size limited and introduce levels of complexity making scaling up of these reactions for broad utilization in green energy applications difficult. Hence the initial goal was to develop a simple scalable method of producing low dimensional FeS_2 nanoparticles. The focus was on taking the previously mentioned short lived intermediates that had the desired dimensionality and used a scalable process and identifying parameters that instead would produce stable 1:2 Fe:S with the same

dimensions. This scalable process would offer a tangible solution to achieve the goal of broad utilization by reducing production effort with the material stability allowing for long term usage.

2.2 Low Dimensional Reaction Pathway

Lowering the reaction temperature of a standard hot-injection iron sulfide synthesis restricted the reaction to its early stages and prevented the formation of the usual three-dimensional (3D) FeS_2 materials. The low temperature slowed the reaction kinetics significantly enough for the observation not only of the structural formation process of the low dimensional materials but also the presence of additional reactions. It was found that prior to the injection of sulfur in the Fe(II) salt/octadecylamine (ODA) ligand solution the Fe^{2+} was being reduced to Fe^0 as seen in Equation 1.

$$Fe^{2+} + 2e^- \xrightarrow{L} Fe^0$$
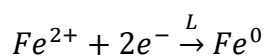
Equation 1. Ligand reduction for the formation of iron seed particles

This led to the formation of small ~3-5 nm Fe^0 nanoparticles in solution and meant that the ODA ligand was acting as a capping layer as well as a reducing agent in the solution. Since the iron in solution had been sequestered into large Fe particles then in order to form iron sulfides they would need to undergo a subsequent oxidation reaction once the sulfur had been injected following Equation 2.

$$Fe^0 + S_x \rightarrow Fe^{2+} + S_x^{2-}$$
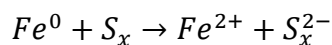
Equation 2. Oxidation of iron seed particles and reduction of sulfur

From here the reactions would follow the previously known reaction pathway producing iron monosulfide (Equation 3) and subsequently iron disulfide (Equation 4).

$$Fe^{2+} + S_x^{2-} \rightarrow FeS + S_{x-1}$$
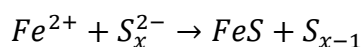
Equation 3. Formation of iron monosulfide intermediate

$$FeS + S_x^{2-} \rightarrow FeS_2 + S_{x-1}^{2-}$$
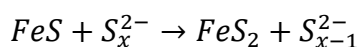
Equation 4. Rate limiting iron monosulfide to disulfide transition

2.2.1 Morphological Control

Using this low temperature reaction method three types of low dimensional nanostructures were produced: 0D Fe nanoparticles, 1D "wires," and 2D "discs." The dimensionality was found to be dependent upon the initial sulfur concentration. Instead of producing a different phase upon increasing the initial sulfur concentration as occurred in the higher temperature reactions forming 3D materials it surprisingly encouraged 2D growth. Therefore by tuning the initial sulfur concentration 1D or 2D growth could be achieved. At a Fe:S ratio of 1:0 (i.e. prior to sulfur injection) iron seed particles formed (Fig 3a). Maintaining a 1:6 Fe:S ratio in the precursor solution produces 1D wires (Fig. 3b). Further increasing the Fe:S ratio to 1:24 promotes the formation of discs (Fig. 3c).
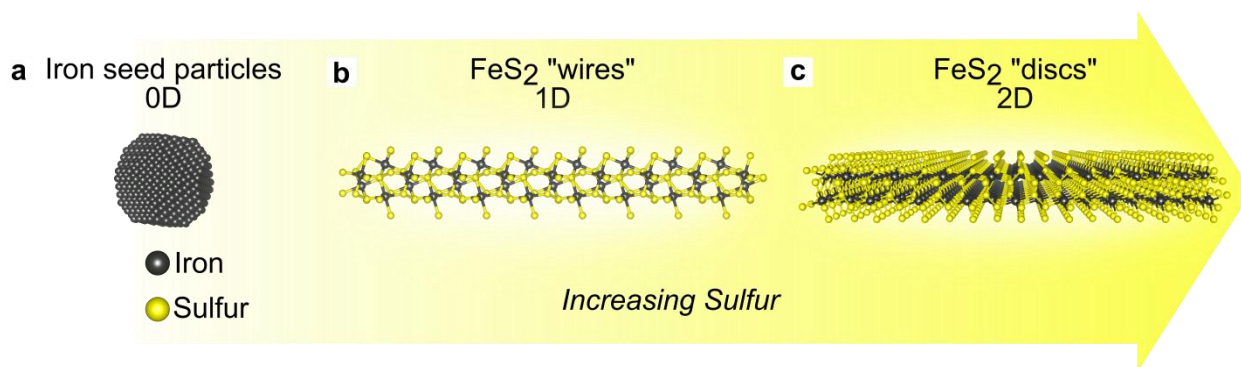
Figure 3. Schematic representation of the different nanostructures formed with varying sulfur concentration.

Both the wires and discs are individually separated from neighboring structures by a compact and uniform ligand layer with a spacing of approximately 2.7 nm as seen in Fig. 4. The separation distance corresponds to the actual size of the ligand assuming an orderly close packed bilayer. This ligand layer allows for the parallel stacking of the individual wires or discs and in the case of the wires there does not appear to be intersections among wire segments.
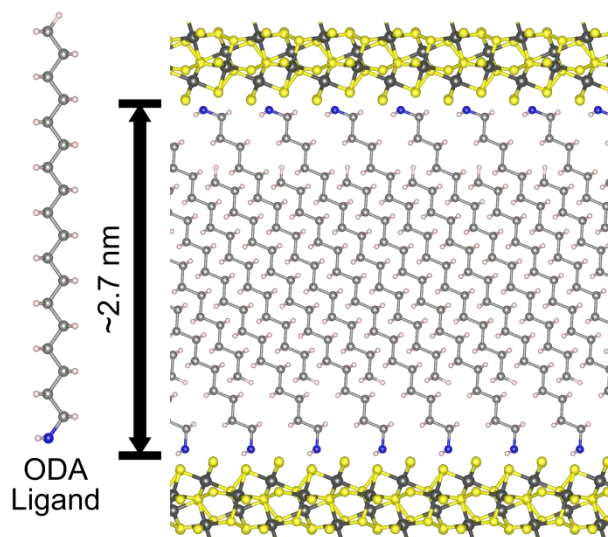
Figure 4. Representation of the ligand interstitial layer separating FeS_2 wire and disc layers causing ordering of them into lamellar-type structures.

The final structures as observed by transmission electron microscopy (TEM) show the large disparity in shape and size between the structures caused by the different growth patterns. The Fe^0 seed particles are mostly spherical and high resolution TEM shows them to be highly crystalline. The wires (Fig. 5b) appear as dark bands on TEM and are on average 1-2 nm in thickness with varying lengths up to several hundred nanometers. Discs as seen in Fig. 5c are extremely thin as seen by the transparency of the structures and individual discs range in diameters from 100 to 400 nm.
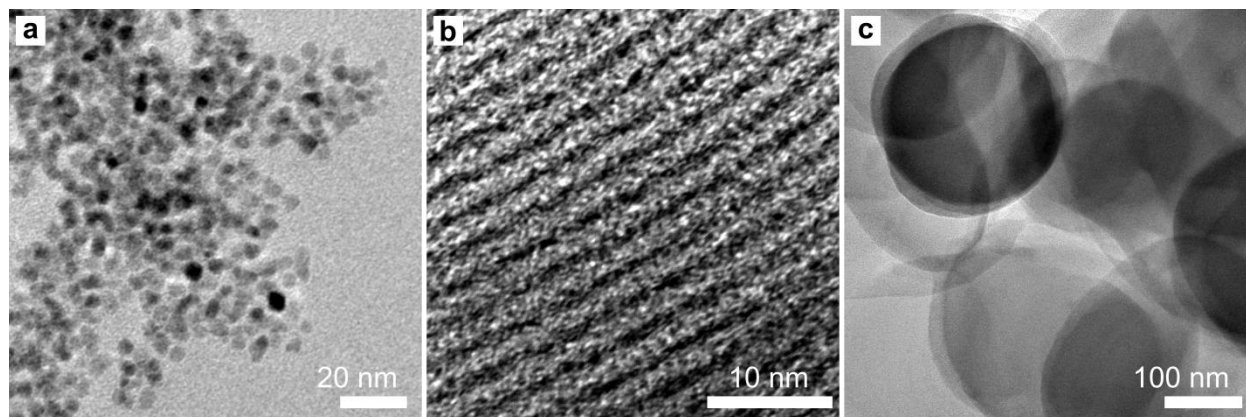
Figure 5. TEM images of (a) zero-dimensional iron seed particles, (b) FeS_2 wire structures, and (c) FeS_2 disc structures.

2.2.2   Wire and Disc Structural Evolution

Using fixed initial sulfur concentrations the time dependent structural evolution of the wires and discs was monitored by TEM. The wire reaction (Fig. 6a-d) appears to have no discernable change in appearance after the first 30 seconds and visible wire formation does not occur until a few minutes into the reaction. The initial particles seen are the Fe^0 seed particles which slowly diminish as the reaction proceeds and have been completely consumed by 60 minutes into the reaction. The reaction was left to run for an additional 3 hours but shows no structural change in comparison to the 60 minute TEM image. Similarly tracking the disc reaction a much quicker reaction is observed. Individual discs begin to form and are visible in the first 30 seconds of the reaction but are still interspersed with large amounts of the Fe^0 seed particles. By 5 minutes into the reaction large disc structures have formed and began stacking and most of the Fe0 has been consumed. Analogous to the wire reaction after 60 minutes all the Fe0 has been consumed and there is no visible structural change in the period between 60 and 240 minutes. In terms of structural formation it should be noted that there does not appear to be a linear growth pathway from 1D to 2D nor is there any observed coalescence of wires to form discs. Wire and disc reactions show visually distinct growth patterns starting from the initial injection at time zero. This suggests that the additional sulfur is disrupting ligand coordination around the iron atom and allowing multidimensional growth which previously had been accomplish through higher reaction temperatures. Also, the different reaction kinetics can be estimated visually by using the presence of the Fe^0 seed particles and following the rate at which they disappear in both wire and disc TEM panels.
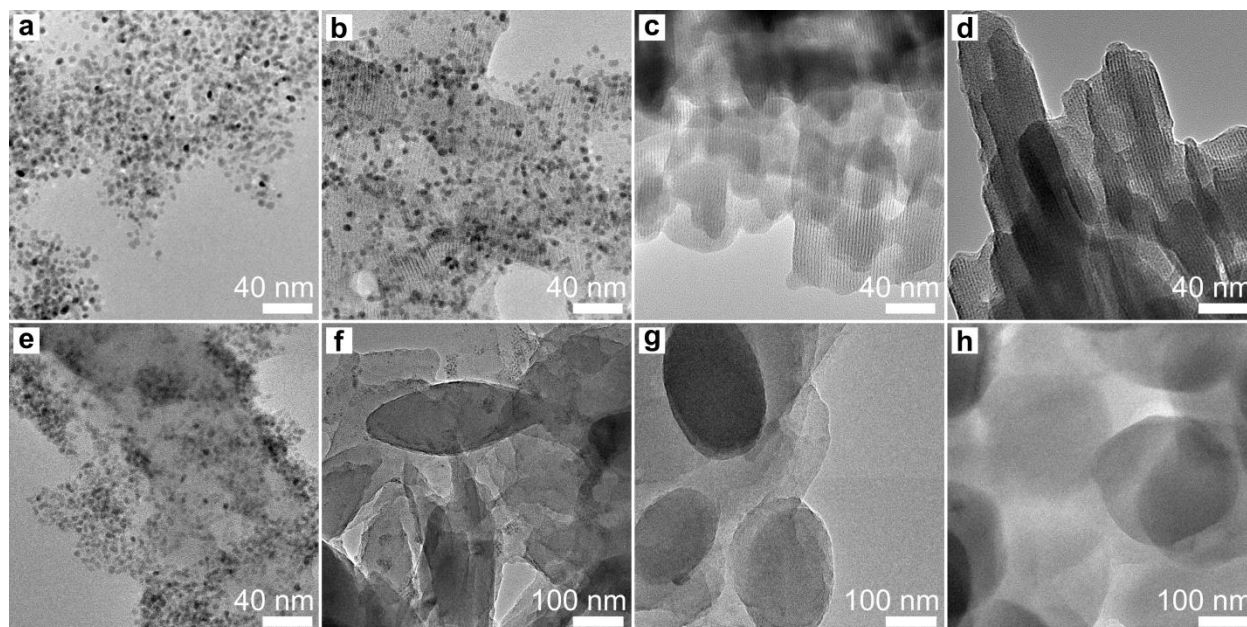
Figure 6. TEM images of aliquots taken at 0.5 min (a,e), 5 min (b,f), 60 min (c,g), and 240 min (d,h).

Characterization of the bulk material performed by scanning electron microscopy (SEM) was used to observe large scale interactions which could affect its intended application as an electrocatalyst. The final wire structure (Fig. 7a) shows the wires forming large sponge-like structures as a result of the ligand-ligand interactions. The wires themselves form bundled strands that span lengths of over a micron with each bundled strand connected to an adjacent one essentially forming one continuous bulk structure. The final disc structure (Fig. 7b) shows the stacking of the individual discs into thicker disc structures likewise held together by ligand-ligand interactions. These thicker disc structures also have increased diameters ranging from 300-800 μm and once again because of ligand-ligand interactions appear to form one continuous bulk structure.
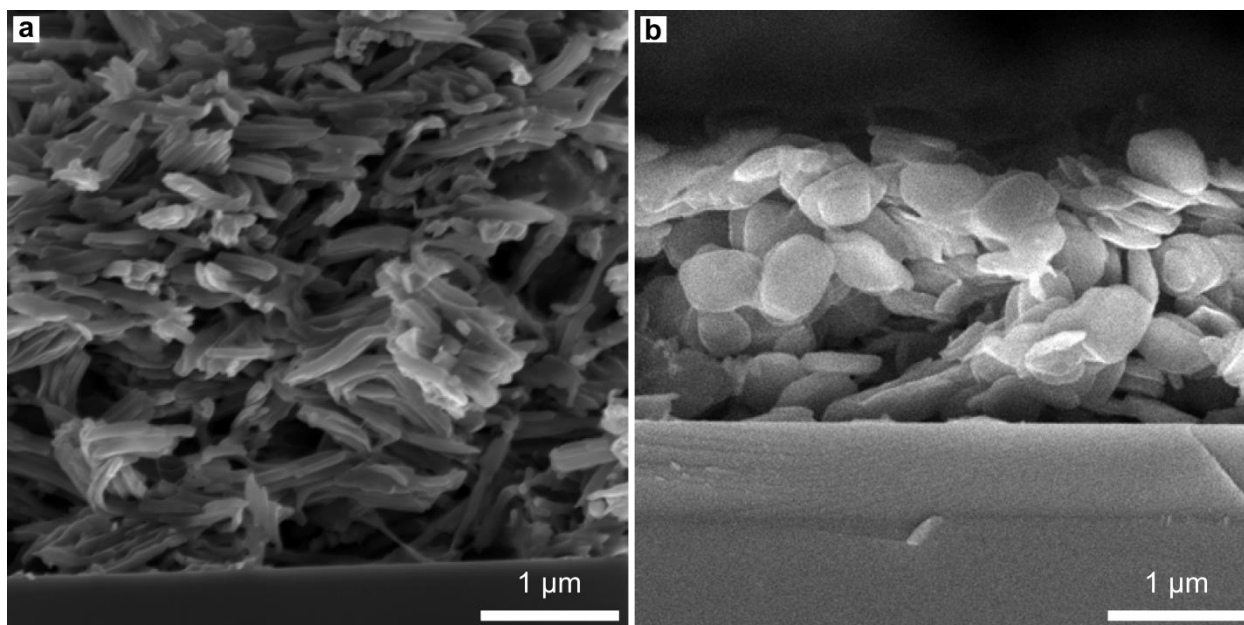
Figure 7. SEM images of (a) wires and (b) discs after 240 minutes as cast on Si substrates.

2.2.3 Stoichiometric Control and Reaction Kinetics

Previous reports of low dimensional materials have typically been non ideal $Fe_{1-x}S$ stoichiometries many of which lack stability as compared to FeS_2.[15] It was found that by simply extending the reaction time both wire and disc reactions would achieve the desired 1:2 Fe:S stoichiometry. These stoichiometric changes over time were monitored via energy-dispersive X-ray spectroscopy (EDS) measurements and are presented in Fig. 8.
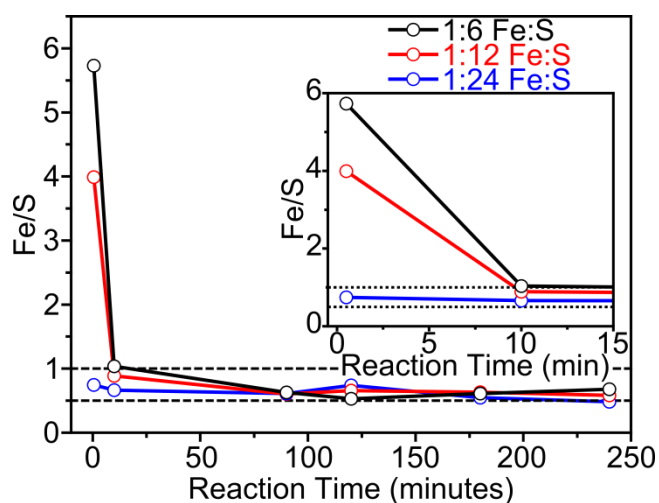
Figure 8. EDS of reactions with various Fe:S precursor ratios. (1:6 Fe:S) corresponds to wire and (1:24 Fe:S) corresponds to discs. The inset magnifies the first 15 minutes of the reaction.

The wire reaction (1:6 Fe:S precursor ratio) initially shows a large excess of Fe close to 6:1 Fe:S caused by the presence of large amounts of Fe^0 seed particles scattered between small amounts of $Fe_{1-x}S$ particles. As these seed particles are consumed there is a rapid drop in Fe and by 10 minutes into the reaction the wires formed are at an approximate 1:1 Fe:S ratio. In comparison to previous work[15] which also saw some of these wire structures the wires presented here during the approximate same reaction time length share a similar 1:1 Fe:S stoichiometry. Since the temperature difference between the reactions is approximately 100°C it could be assumed that the conversion of starting materials to iron monosulfide is not appreciably temperature dependent. After approximately 60 minutes into the reaction the stoichiometry shows an approximate 1:2 Fe:S ratio which corresponds well to the TEM images which show no excess Fe^0 and an unchanging structure from 60 minutes onward. In contrast the disc reaction (1:24 Fe:S precursor ratio) initially does not show such a gross excess of Fe even though visually Fe seed particles can be seen by TEM. The initial stoichiometry is closer to 1:1 and shortly thereafter reaches 1:2. Once again in reference to TEM the disc structures can be seen in the initial TEM images and be closer to a 1:2 Fe:S stoichiometry but the presence of the Fe^0 seeds is initially distorting the actual ratio. From this data as well as the TEM images it appears that a minimum reaction time of 90 minutes is necessary to achieve a 1:2 Fe:S stoichiometry for final products.

In addition to monitoring stoichiometric changes this EDS data can also allow the measurement of reaction kinetics by monitoring the rate at which the Fe:S ratio changes over time. This indicates that the lower the initial sulfur concentration the slower the reaction proceeds and at sulfur concentrations near that of the discs the reaction proceeds rapidly with large structural formation occurring in less than 30 seconds.

The EDS kinetics data is further supported by UV-Vis-IR absorbance measurements.

UV-Vis-IR measurements were taken of aliquots of wire and disc reactions at 0.5, 5, 10, 30, 90, and 240 minutes. Initially peaks are not readily apparent, but after reaction times greater than 1 minute the characteristic peaks appear at 320, 430, 530, 660, and 700 nm in both the wire (Fig. 9a) and the disc (Fig. 9b) reactions. Optically the 2-D growth of the discs causes rapid peak formation with little difference between scans at earlier and later reaction times. The 1D growth of the wires shows slower peak formation, and the resulting spectra is similar to those previously reported when investing growth of other pyrite structures where the wires were an intermediate stage. In the early stages of the wire reaction, the shorter wavelengths dominate the spectra and have the highest relative intensities. However, as the reaction progresses, the peaks at 660 and 700 nm proceed to become the dominant peaks with the 700 nm peak appearing as a lower intensity shoulder. The absorbance spectra stabilize when the 700 nm shoulder eclipses the 660 nm peak achieving the highest maximum relative intensity of all the characteristic peaks.
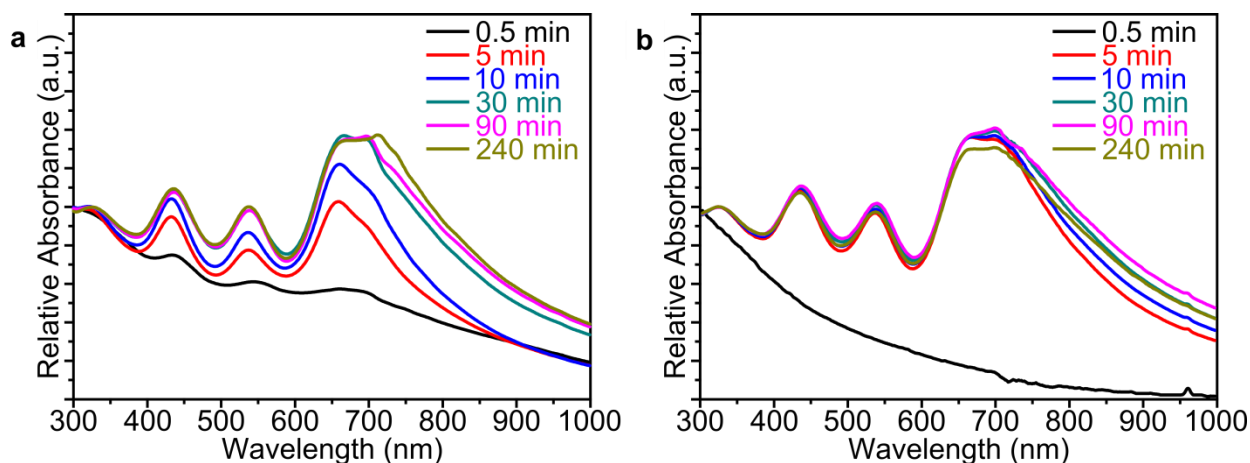
Figure 9. Time dependent UV-Vis-IR absorbance spectra of (a) wires and (b) discs

This spectral stabilization can be plotted to better illustrate the reaction rate differences and such plots for wires (Fig. 10a) and discs (Fig. 10c) are shown below. The point at which the 700 nm peak becomes dominant correlates to the final structural formation and can be seen as reaching the 1:2 stoichiometry. These plots do not completely match timescales most likely because of EDS measurements taking into account Fe^0 while the iron is not contributing to the

absorbance seen at all so it is $Fe_{1-x}S$ dependent. Additionally, the growth of the 700 nm absorbance peak over the course of the reaction was plotted (Fig. 10c) and shows a strong correlation with the EDS data monitoring stoichiometry. The fact that the 700 nm peak grows in and does not appear to shift as it grows suggests a structural (i.e. stoichiometry) change instead of a size dependent shift in peak absorbance because of confinement. Also, the rate and time at which the 700 nm peak reaches its maximum could be used as an in-situ method for characterizing wires or discs formation as well as reaction progress, respectively.
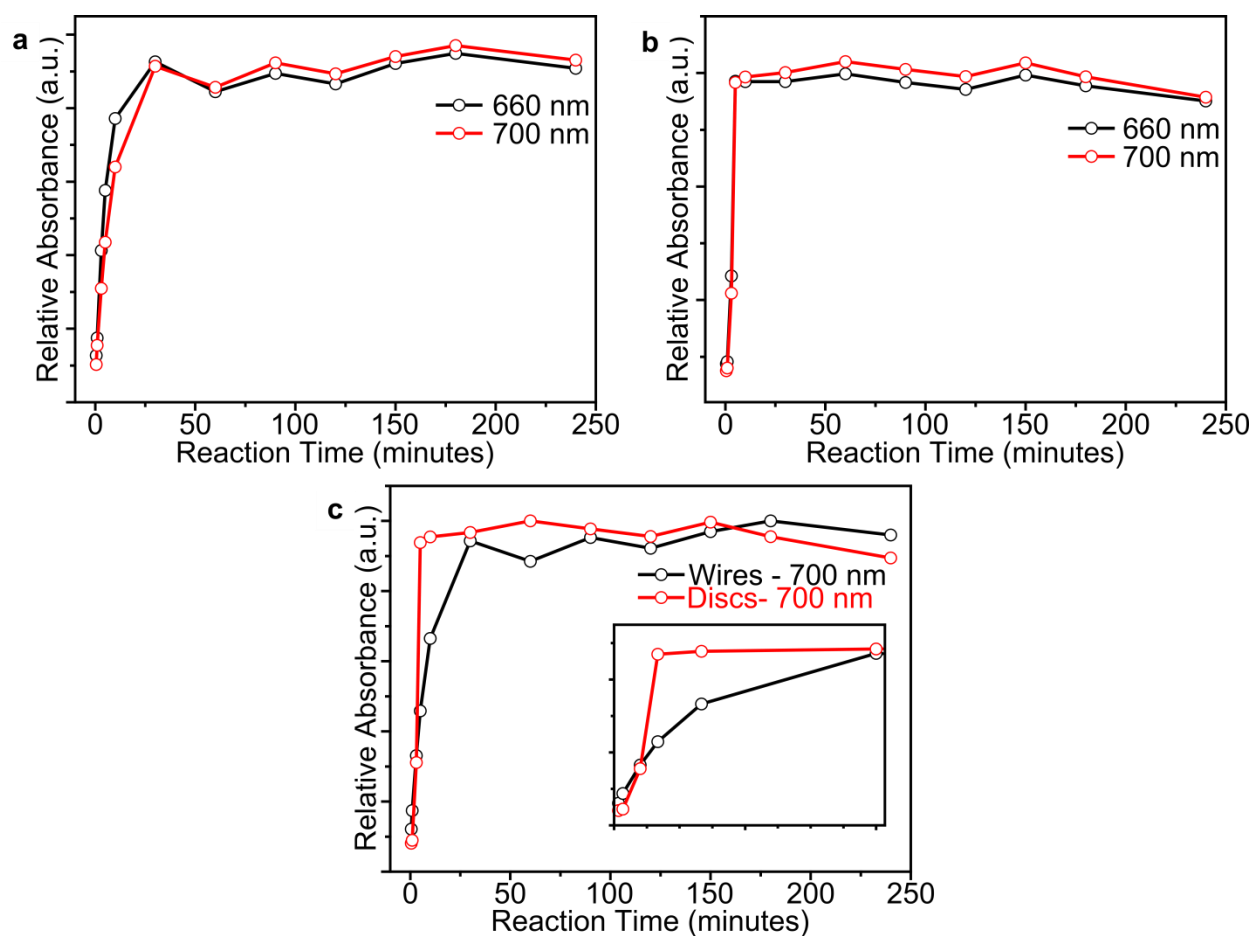
Figure 10. Time dependent relative peak height comparisons of the 660 and 700 nm peaks of (a) wires and (b) disc reactions. (c) is time dependent relative peak height comparison between both wires and discs. The inset in (c) shows a magnified view of the initial 30 minutes of the reaction

2.2.4   Structural Characterization and Phase Identification

Different crystal structures exist for FeS_2 and since these low-dimensional materials have

not been previously made before with a 1:2 Fe:S stoichiometry it is important to identify which

phase or phases are present. To help clarify structure Raman spectroscopy was used and the

results are presented in Fig. 11. Both the wire and disc structures share a characteristic set of

Raman peaks at 291 and 358 cm^{-1}.[20,21] These peaks commonly appear in other FeS_2 reactions in

the early stages but usually disappear as the reaction progresses.[16] In this case the thinness of

these 1D and 2D materials may not allow for the more typical Raman active modes of the usual

FeS_2 phases (e.g. pyrite, marcasite) nor of the other typical $Fe_{1-x}S$ phases. However, the

combination of the EDS stoichiometry data and the presence of highly ordered nanostructures

visible in the TEM images lead to the conclusion that these peaks correspond to an ordered FeS_2

structure.
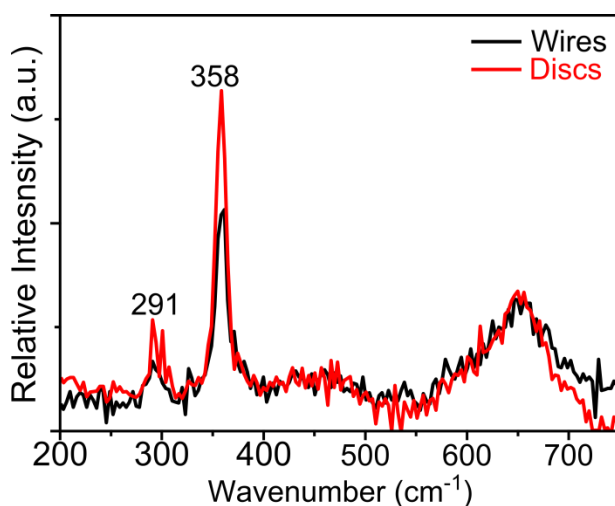
Figure 11. Raman spectra of wires and discs

Further structural characterization of the materials by X-ray diffraction (XRD, Fig. 12)

was used to determine phase and follow structural evolution during the course of the reaction.

Samples tested after 1 minute confirmed the formation of crystalline Fe nanoparticles prior to

sulfur injection as well showed their persistence as the reactions progressed. The Fe peaks match

to Fe_2O_3 (Fig. 12a,b) as a result of exposure of these small particles to open air during the

measurement. The differences in the rates of Fe seed consumption rates are evident here as well

with prominent diffraction peaks seen for the wires (Fig. 12b) but subtle peaks seen in the discs (Fig. 12a). As the reaction progressed, the iron oxide peaks disappeared and what is left is mostly noise with small peaks observed that do not match with the typical 1:2 Fe:S structures of iron pyrite or marcasite. Numerous other Fe_xS_y XRD patterns were investigated but none matched appropriately. This may be caused by the limitations of the XRD when scanning particles with atomic layer dimensions leading to insufficient scattering volume and thus too low of a signal.
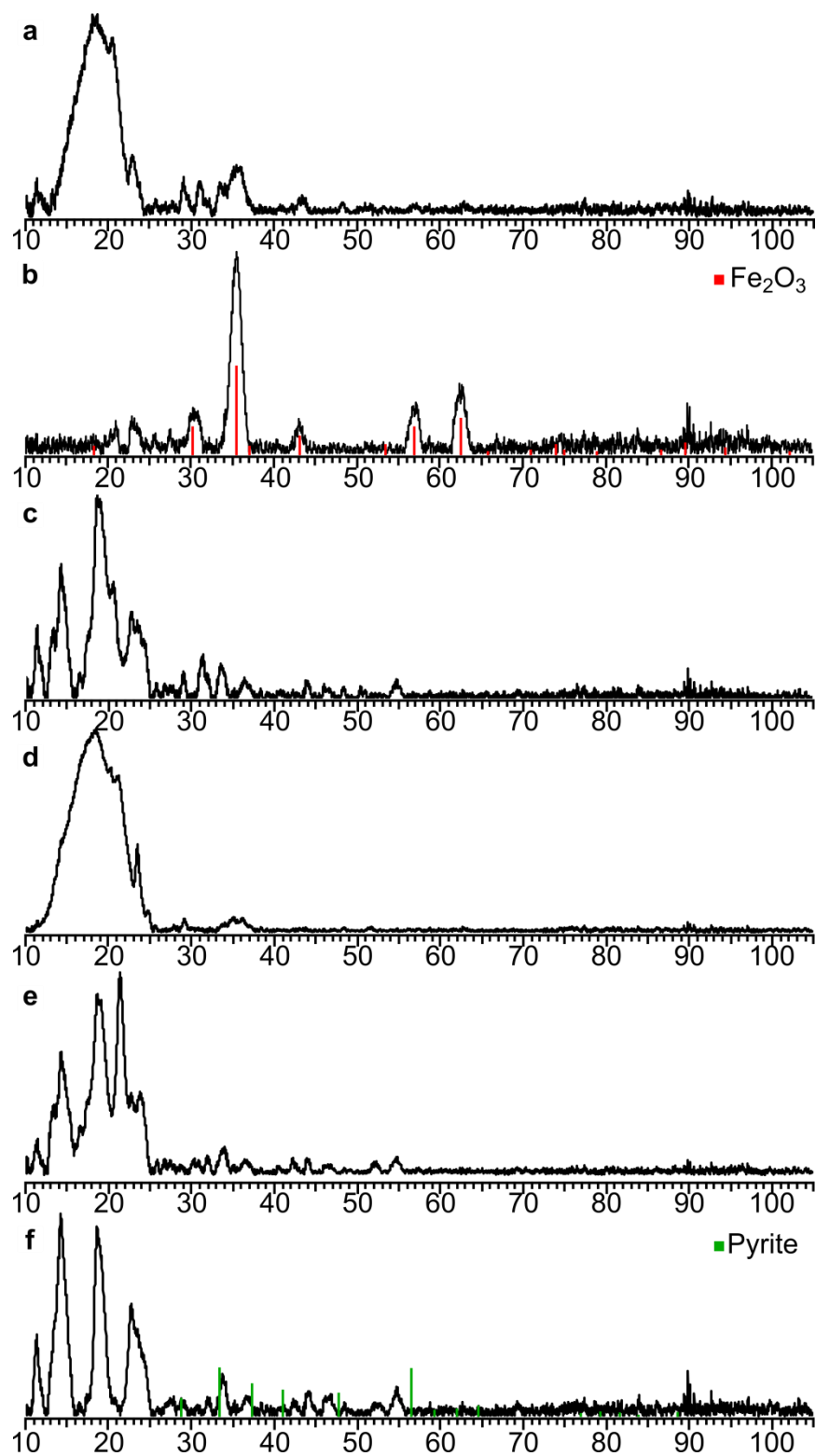
Figure 12. X-ray diffraction of discs (a,c,e) and wires (b,d,f) taken at reactions times of 1 min (a,b), 30 min (c,d) and 240 min (e,f). The red peaks correspond to Maghemite, Fe2O3 (00-004-0755) and the green peaks correspond to Pyrite, FeS2 (00-001-1295)

16

Confirmation of the presence of ligand in the interstitial layers between wires and discs was done by Fourier transform infrared spectroscopy (FTIR) and data taken of the different samples suggests a large amount of residual ligand in both wire and disc samples. These FTIR bands associated with ODA remain in these materials even after extensive washing. Since the interlayer between the individual wires or discs is supposedly ODA, ODA peaks should appear and are visible in the spectra (Fig. 13).
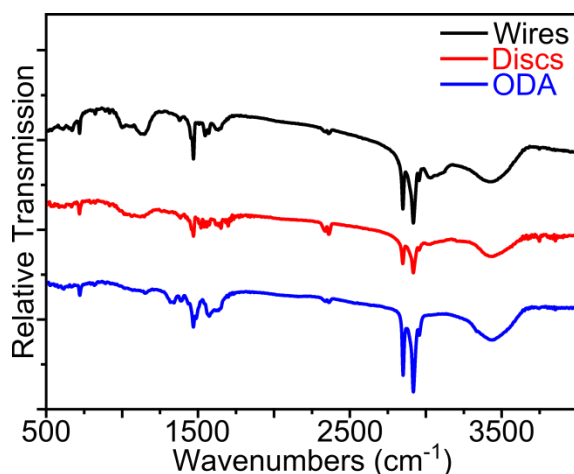
Figure 13. Comparison of FTIR spectra showing the presence of residual ODA ligand in both wire and disc samples.

2.3   Revisions to the FeS$_2$ growth model

Clearly this approach to making FeS$_2$ nanostructures does not follow the normal reaction pathway as described by the combination of La Mer theory, Ostwald ripening (OR), and oriented attachment (OA). In fact there appears to be to separate nucleation and growth events that occur in the formation of the 1D and 2D structures with the first being the formation of Fe seed particles and the second being the formation of the actual FeS$_2$ structures. Since the reaction is operating at a low temperature it was thought that the transition to higher order structures was limited by a kinetic barrier that prevents Ostwald ripening and OA growth from occurring. In previous work that has shown the formation of FeS wire structures it was assumed that they were some intermediate phase and subsequently annealed at high temperatures (~500°C) to form large

17

crystals FeS_2 crystals. If this were a true intermediate phase then increasing the reaction temperature after forming these 1D and 2D structures should allow for the transition of these materials from 1D→2D→3D materials. Understanding this fundamental reaction pathway would be beneficial not only for the 1D and 2D structures but could allow for a better understanding of defects in higher order structures that are targeting other applications such as the solar or battery market. To test if this low temperature reaction allowed for an alternate pathway or it was only an intermediate phase the wires and discs were grown and then heated to normal FeS_2 reaction temperatures.

2.3.1   Temperature Dependent Structural Evolution

A standard wire reaction was run for 90 minutes to form stable FeS_2 wires then the temperature was quickly increased and the reaction was allowed to continue for the rest of its 240 minute reaction time. The rationale behind choosing these timescales was based on the data presented earlier showing that stoichiometry and structure essentially go unchanged after 90 minutes and prior work indicating that 3-D particle formation occurs within 90 minutes in the high temperature reactions. The reactions were varied by ~30°C increments using 120°C as a baseline and 220°C as the upper limited giving data points at 120°C, 160°C, 190°C, and 220°C.

TEM images taken at 160°C (Fig. 14a-d) show the initially formed wires gradually change from visible strands to thinner shorter strands with less distinction between them. Also, small spherical particles approximately 2-4 nm in diameter appear intermixed with the wire structures. At 190°C (Fig 14e-h) a much more distinct change in the wire reaction is seen. Visibly wires begin to smooth out by the 120 minute mark and by 180 minutes the wires have become large thin sheets with small particles once again scattered around them. By the end of the reaction there is visible evidence of Ostwald ripening and even oriented attachment growth occurring to form larger particles. Once the reaction is increase to 220°C (Fig. 14i-l)seed

particles are visible at the 120 minute mark and once again there is visible evidence of these particles undergoing OR and OA growth. These 3D cubes that form appear to be encased in the thin sheets that formed earlier in the reaction. The disc reaction run at 220°C (Fig. 14m-p) shows once again a much faster transition showing large amounts of seed formation early in the reaction and cube formation by 180 minutes. In contrast to the wires there are no residual thin sheets present at the end of the disc reaction.
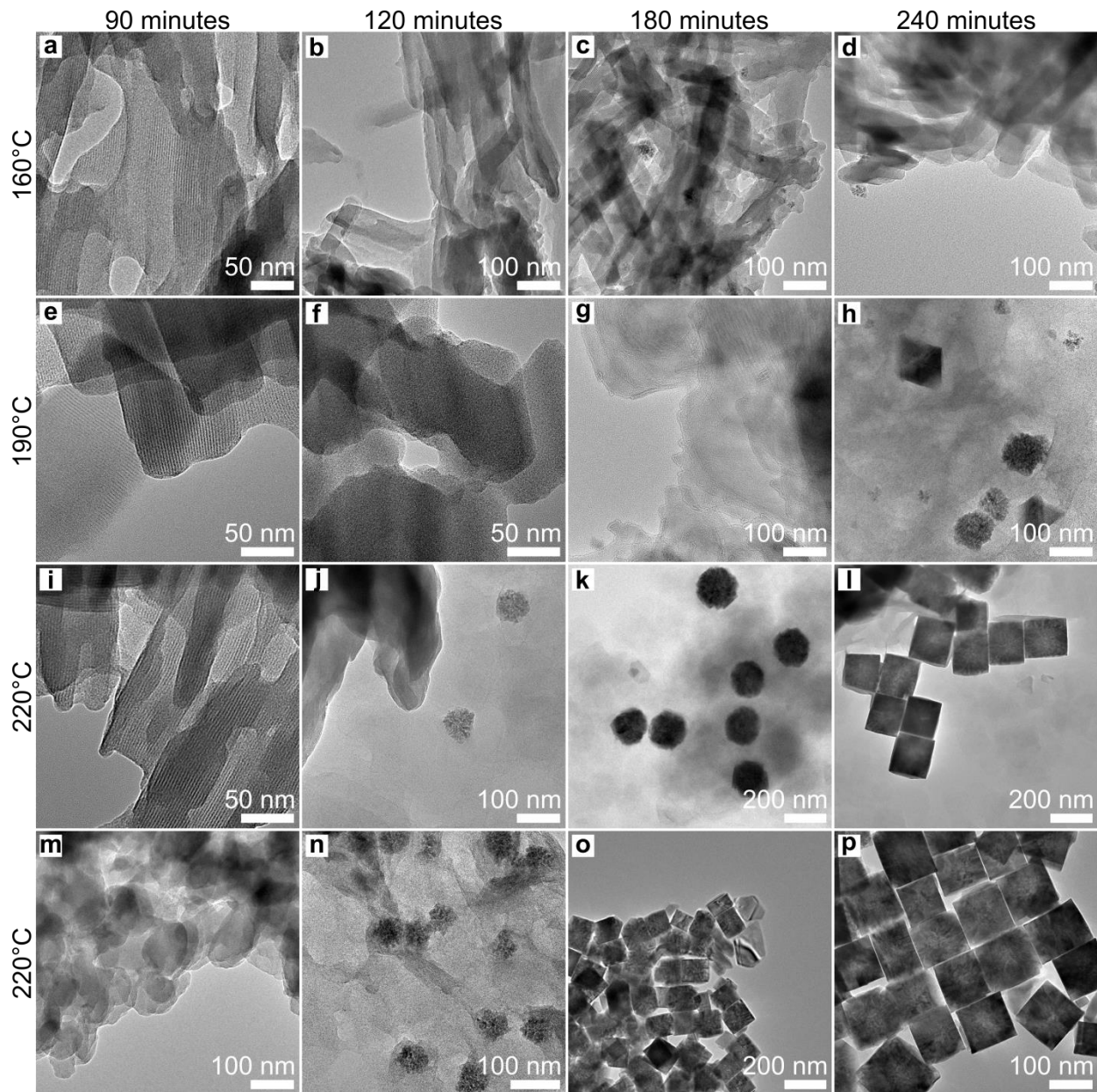
Figure 14. TEM images of the wire reaction at 160°C (a-d), 190°C (e-h), 220°C (i-l) and Disc reaction at 220°C (m-p). Images from left to right are taken at 90, 120, 180, 240 min, respectively.

Examination of the bulk structures by SEM reinforces what was seen in the TEM images. Discs (Fig. 15a) produce clean sets of cubes with a fairly narrow size distribution while the wire reaction (Fig. 15b) produce a lesser amount of cubes embedded in what appear to be platelet-like structures which seem to correspond to the thin sheets observed in TEM.
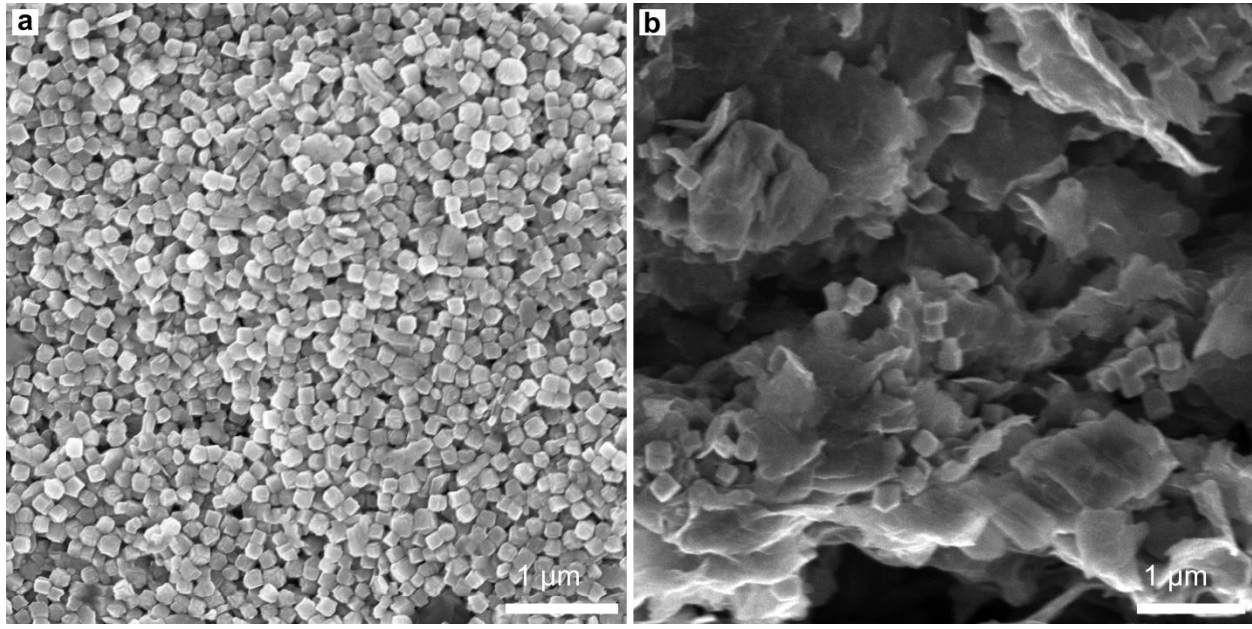
Figure 15. SEM images of (a) disc and (b) wire reactions at 220°C after 240 minutes

The TEM and SEM data seem to contradict previous assumptions that these low-dimensional structures are intermediates. If these structures were true intermediates they would coalescence or self-assemble in some way into the larger higher dimensional nanostructures such as plates, spheres, or cubes. Instead they appear to gradually disintegrate and undergo a second nucleation and growth period followed by oriented attachment to form cube structures.

2.3.2   Stoichiometric Differences and Reaction Kinetics

Time and temperature dependent stoichiometric differences as well as reaction kinetics were tracked by EDS to note any similarities between these higher temperature reactions and the 1D and 2D reactions. Fig 16a illustrates the changes in composition at increasingly higher temperatures for the wire reaction. It appears as if instead of breaking apart into smaller FeS_2 subunits to undergo OR and OA the iron goes through additional redox steps to then form what would be a third nucleation and growth period as seen by the spike in relative Fe concentration. Interestingly, reaction temperatures below 220°C appear to shift the third nucleation step to longer reaction times. However in the case of the 160°C reaction it is unknown if it did not have enough energy to overcome the kinetic barrier preventing this third nucleation step or the

21

reaction time was not adequate enough to witness it. Comparison of the disc and wire reactions at 220°C (Fig 16b) once again illustrates the much faster kinetics present in the disc reaction. The lower Fe/S peak suggest that either the iron is being consumed more rapidly and therefore high Fe concentrations can never be achieved or that the relative maximum lies between when first 2 data points. The presence of large amounts of seed particles seen after 120 minutes seems to indicate that the latter explanation is the realistic cause.
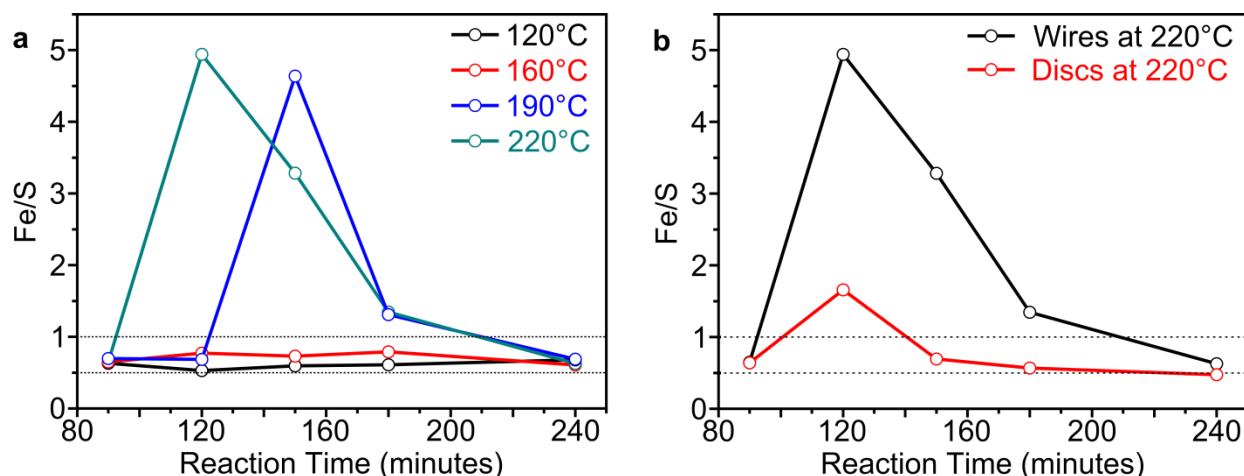
Figure 16. Temperature dependent EDS measurements for the wires are shown in (a). EDS data plotted in (b) shows the comparison of wires and discs at 220°C

Differences in observed reaction kinetics may also be caused by a combination of several other factors. The wires as seen in both TEM and SEM images are resistant to this disintegration and leave extremely thin platelet like structures interspersed with cubes. As seen in the low temperature reaction the disc reaction proceeds quicker than the wires so it would make sense that the discs would undergo the disintegration and reformation steps more quickly. Additionally, the presence of the ligand as the interstitial layer in the wires may be acting as a barrier layer preventing rapid dissolution as several layers sit between the wires and the surface exposed to solution.

The effects on the optical characteristics are illustrated in Fig. 17 where both reactions rapidly lose the characteristic set of 5 absorbance peaks. The wire reaction (Fig. 17a) maintains

absorbance in the lower wavelengths but characteristic low dimensional absorbance peaks they smooth out to form a broad absorbance peak that extends into the near-IR (NIR) region. Only at the end of the reaction at 240 minutes is the NIR peak which is characteristic of cubes observed (weakly). The wire reaction retains some small amount of the absorbance most likely caused by the high abundance of thin wire-like material present. The disc reaction (Fig. 17b) never develops the broad absorbance peak seen in the wire reaction and instead shows the formation of IR peaks initially at 1000 nm which as the cubes grow red shift to 1200 nm which is consistent with the formation of cubes.
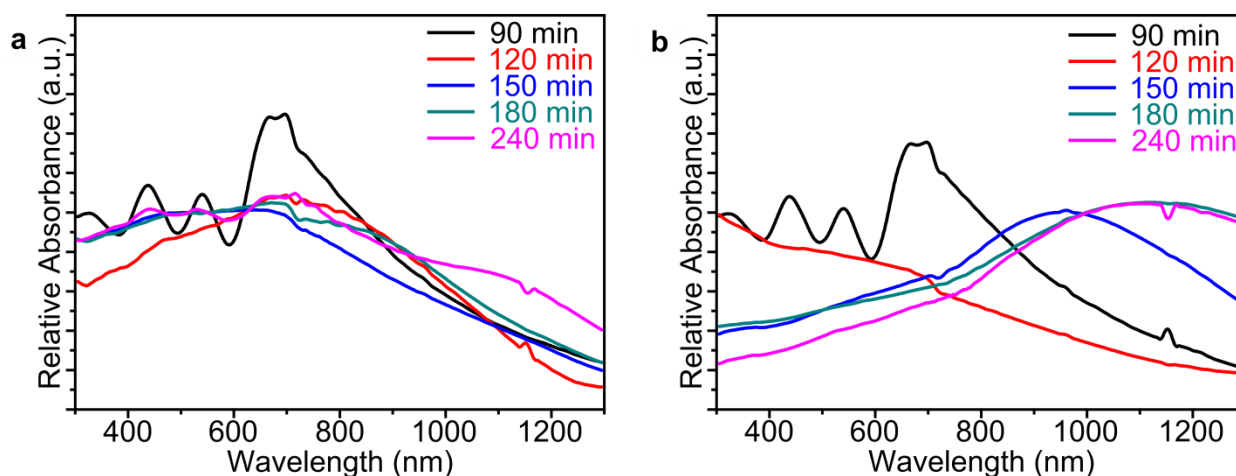
Figure 17. UV-Vis-IR spectra taken of (a) wire and (b) disc reactions starting at 90 minutes

2.4   Conclusions

Hyperthin low-dimensional FeS_2 nanostructures were prepared via a low-cost and scalable solution processing method. Tuning of the dimensionality of the structures between 1D and 2D was found to be dependent on the initial sulfur concentration and a 1:2 Fe:S stoichiometry could be achieved by simply increasing reaction time. Investigation of the 1D and 2D reaction pathway has shown that these low dimensional nanostructures are not reaction intermediates as previously thought but instead are the product of side reactions that occur in the initial stages of the reaction. Furthermore these low dimensional materials do not undergo Ostwald ripening or orientated attachment as a result of confinement by a high temperature

23

kinetic barrier. Additionally how these side reactions sequester the Fe and S have a significant impact on the final product which is crucial to understanding the formation of subsequent structures. Finally, design of these high surface area materials in stable phases is essential for development of these materials as electrocatalysts.

2.5   Materials and Methods

2.5.1   Materials

FeI_2 (Sigma-Aldrich, anhydrous, $\geq$99.99%), sulfur powder (Sigma-Aldrich, Colloidal), octadecylamine (Acros Organics, technical grade, 90%), diphenyl ether (Acros Organics, 99%), chloroform (BDH, Anhydrous), methanol (Fischer Chemical, ACS), tetrachloroethylene (Sigma-Aldrich, ACS) were all used as received.

2.5.2   Wires and Discs Synthetic Procedure

To make the FeS_2 wires, 0.5 mmol of FeI_2 and 1 mL of phenyl ether was added to a septa sealed vial in a N_2 flushed glovebox. This mixture was sonicated to form a uniform slurry, approximately 1 hour. In a round bottom flask 12 g of ODA was added and degassed and backfilled with argon. The flask was then heated to 120°C, degassed and backfilled with argon again, and allowed to cool to ~80°C. The FeI_2 precursor solution was injected into the flask containing ODA and heated back to 120°C and then left to stir for 1 hour to allow the precursor to decompose. In a separate flask, 128 mg of sulfur and 5 mL of phenyl ether was added and then degassed and backfilled with argon. This flask was heated to 70°C and left to stir for 1 hour. After 1 hour, the sulfur solution was rapidly injected into the Fe-ODA solution and left to react at 120°C for 4 hours. The solution was allowed to cool to ~100°C before injection of 10 mL of chloroform to prevent the solution from congealing and then was transferred to centrifuge tubes, topped off with methanol, and centrifuged at 4000 rpm for 7 minutes. The supernatant was poured off and an additional 5 mL of chloroform and 40 mL of methanol was added the solution

mixed and was centrifuged again. This step was repeated two more times resulting in a fluffy black solid that was suspended in chloroform and stored under nitrogen. The same procedure is used to make discs except only 0.125 mmol of FeI_2 was used.

2.5.3   Characterization Methods

UV–Vis absorbance spectra were taken on a UV-3600 Shimadzu UV–Vis–NIR spectrophotometer with all samples being dispersed in tetrachloroethylene. X-ray powder diffraction was done at room temperature using monochromatic Cu-Kα radiation on a Brukerproteum diffraction system equipped with Helios multilayer optics, and APEX II CCD detector and a Bruker MicroStar microfocus rotation anode X-ray source operating at 45 kV and 60 mA. Powders were suspended in Paratone N oil and placed into a nylon loop and mounted on a goniometer head. TEM images were obtained using a field emission FEI Tecnai F20 XT 200kV Field Emission Transmission Electron Microscope. EDS spectra were acquired using an EDAX SiLi detector. SEM images were obtained using a Zeiss LEO 1550 Field Emission Scanning Electron Microscope. Fourier transform infrared spectroscopy (FTIR) was performed using a Nicolet 6700. Raman spectroscopy was performed using a Witec alpha 300 with a 633 nm wavelength laser.

3   FeS$_2$ Electrocatalysts

3.1   Motivation

Many different materials have been investigated attempting to identify effective replacements for precious metal electrocatalysts.[22-24] One class of materials that has received a large amount of attention for this purpose is that of nanostructured transition metal dichalcogenides such as WS_2, NiS_2, CoS_2, $NiSe_2$, MoS_2, and $CoSe_2$.[25,26] Several of these have shown promising results as HER electrocatalysts however they still suffer from problems with not only efficiency and stability but a lack of available synthetic routes leading to an overall

reduced cost effectiveness. As an example, 2D MoS_2 which is one the most studied metal

dichalcogenide catalysts has limited efficiency because only the edge sites have appreciable

activity.[27-29] However, the metal dichalcogenide FeS_2 nanostructures are orders of magnitude

less expensive and have a variety of facile synthetic routes. Nevertheless, there have been

limited reports on the catalytic activity of FeS_2 for the HER, and none have shown high

electrocatalytic activity for FeS_2 structures.[23,26] The objective was to develop the high surface

area, stable-phase, and low-dimensional FeS_2 materials into effective HER catalysts and identify

which structure offers the best performance.

3.2   Catalytic Performance of 1D and 2D materials

Measurements involving electrocatalytic performance, stability, and the confirmation of

hydrogen evolution were conducted in collaboration with Dr. Kevin Leonard and Joe

Barforoush. Electrocatalytic activity for 1D wire, 2D disc, and 3D cube FeS_2 nanostructures

was tested using linear sweep voltammetry in a neutral pH buffered solution. Multiple runs with

each type of nanostructure show little variability within each type but do not show overlap

between runs of different structures as seen in Fig. 18a. Calculating theoretical active area of

each structure the 1D wires should have performed the best followed closely by the 2D discs but

surprisingly from these experiments the 2D structure had the highest electrocatalytic

performance. The low performance of the wires may be caused by the presence ligand-ligand

interlayer and formation of bundled strands are most likely limiting access to the wires active

sites. Additionally a platinum electrode was run using the same conditions as the FeS_2

nanostructures to compare performance and a bare glassy carbon electrode was run as a control.

Data from the highest performing wire, disc, and cube runs were plotted alongside the platinum

and carbon electrode data and can be seen in Fig. 18b. The increase in current as the voltage is

swept from positive to negative potentials is known as the hydrogen evolution onset potential

and indicates the potential at which hydrogen formation occurs. The onset potential for both platinum and the FeS$_2$ discs are similarly low indicating higher efficiency while the other structures show higher and higher potentials signifying lower and lower efficiency with the bare carbon electrode lacking an onset potential completely. This experimental onset potential for both platinum and the FeS$_2$ discs is near the theoretical onset potential signifying a low overpotential and further confirming the high efficiency of the materials.
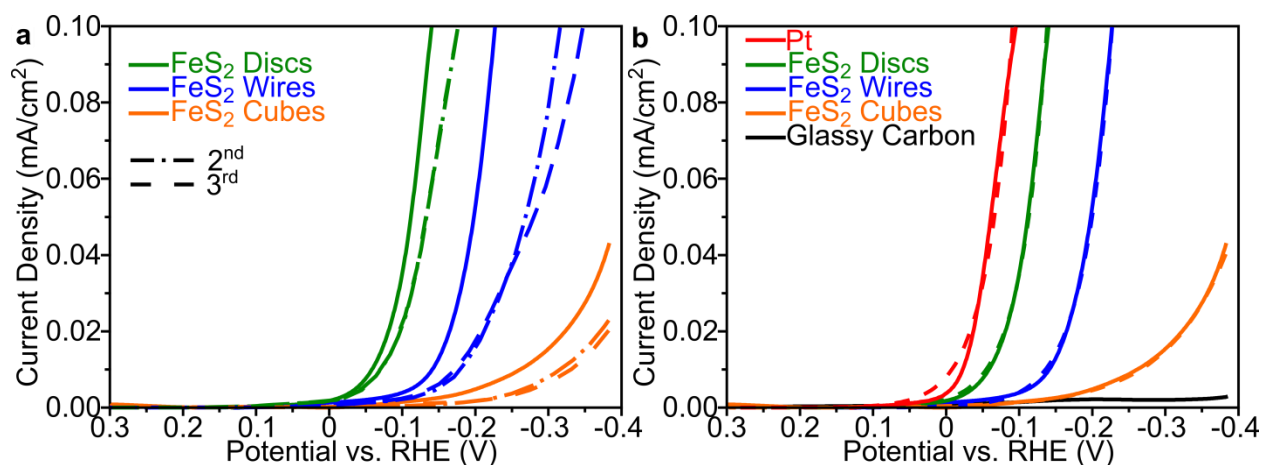
Figure 18. Linear sweep voltammetry measurements of wires and disc structures as well as reference materials. (a) contains the results of triplicate runs denoting highest performance and "2nd" and "3rd" best runs (b) contains highest performance experimental data (solid line) and Butler-Volmer fit data (dashed line) (data generated by collaborator J. Barforoush).

To quantify the electrocatalytic activity, the experimental data was fit (dashed lines, Fig. 18b) to the single-electron transfer Butler-Volmer equation[30] (Equation 5) assuming no mass transfer effects.

$$j = j_0 e^{-\alpha f \eta}$$

Equation 5. Butler-Volmer equation

Here j is the current density, j_0 is the exchange current density, α is the transfer coefficient, f is the faraday constant and, η is the overpotential. The exchange current densities, j_0, for the FeS$_2$ discs, wires, and cubes were determined to be 2.2, 0.32, and 0.41 μA cm^{-2}, respectively. Higher exchange current density for the discs corresponds to higher catalytic

activity.[30] The transfer coefficients, α, were determined to be 0.71, 0.65, and 0.31 for the FeS_2

discs, wires, and cubes, respectively. For comparison, the exchange current density and transfer

coefficient were also determined for platinum equation and came out to be 8.0 µA cm^{-2} and 0.71,

respectively. Similar values obtained for the discs and platinum once again indicate that FeS_2

discs have an overall efficiency comparable to platinum.

In addition to high performance these discs must also be stable if they are to be used as

electrocatalysts. To determine the stability of the FeS_2 discs, a sample was prepared on an

electrode and a constant potential of -0.14 V vs RHE was applied for over 125 hours in a

buffered neutral pH solution while stirring. The reduction current was measured as a function of

time and Fig. 19 shows that the reduction current did not change significantly over the 125-hour

experiment. Degradation of the electrocatalytic performance would be observed as a negative

trending slope which is not observed. Oscillations in the current are caused by outside vibrations

while some of the larger dips are caused by the nucleation of bubbles in solution causing

temporary drop in current until the bubble is eliminated. This suggests that the FeS_2 discs can

stably generate hydrogen for long periods of time if when held at negative potentials.
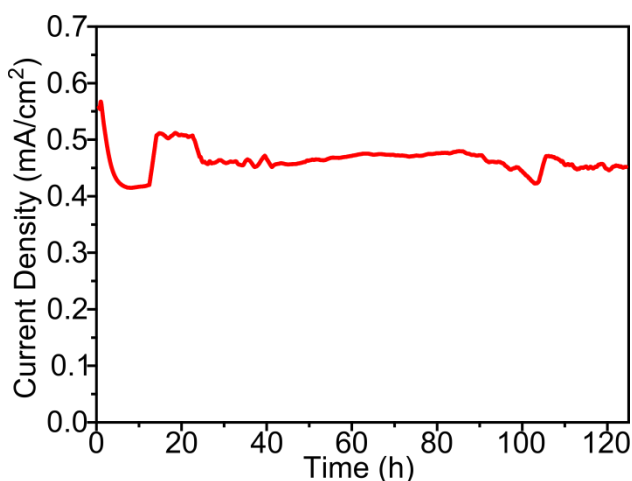
Figure 19. Stability measurement for 125 hour period under constant negative potential (data generated by collaborator J. Barforoush)

3.3   Verifying hydrogen evolution

There is a possibility for chemical reactions to occur and skew results by generating false positives therefore to ensure that the material itself was responsible for generating hydrogen a technique known as scanning electrochemical microscopy (SECM) was employed..[31-34]

3.3.1   Scanning Electrochemical Microscopy (SECM)

Electrochemical reactivity maps were obtained via SECM (Fig. 20) to verify that hydrogen was evolving from the FeS_2 surface. Fig. 20a shows the SECM schematic for obtaining a hydrogen evolution electrochemical reactivity map. The catalytic electrode was held at a reductive potential to generate hydrogen, and a SECM tip electrode (platinum) was held at an oxidative potential to oxidize the hydrogen back to protons. The SECM tip was rastered above the catalyst electrode and the tip current was recorded as a function of position. Hydrogen generation by the catalyst electrode produces current and areas of high current appear as red on the color scale while areas with little or no current appear as blue.
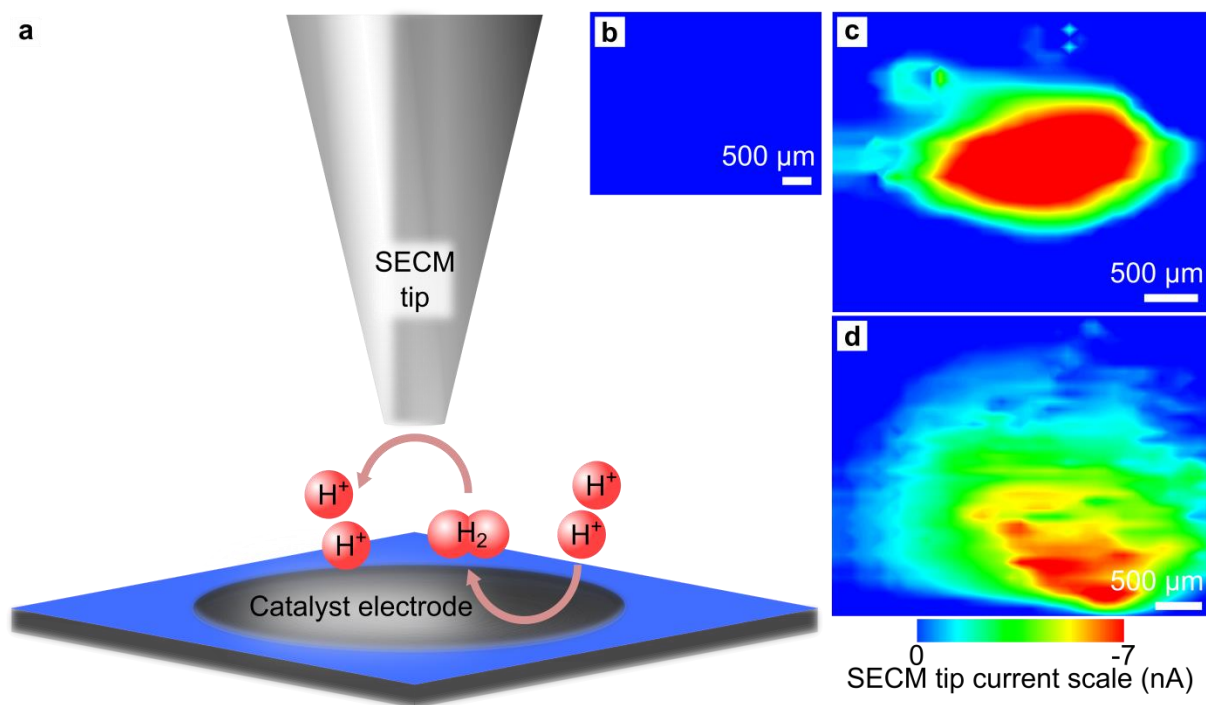
Figure 20. SECM setup (a) illustrating hydrogen generation and collection. (b) is the control run with bare glassy carbon electrode. (c) and (d) are the HER reactivity maps for Pt and FeS_2 discs, respectively (data generated by collaborator J. Barforoush).

As a control to ensure negligible contributions of hydrogen generation by the substrate electrode and electrochemical reactivity map was generated with a bare glassy carbon electrode as seen in Fig. 20b. In this case, without the FeS_2 discs, no oxidation current was recorded on the tip electrode under an applied potential, which demonstrated that no hydrogen was present in solution when only the bare glassy carbon electrode was used. As a reference, an electrochemical reactivity map for the HER on a platinum electrode was obtained (Fig. 20c) and shows significant current which indicates the presence of hydrogen. The HER electrochemical reactivity map for the FeS_2 discs electrode (Fig. 20d) also shows a significant current, thus, via these SECM electrochemical reactivity maps, we can conclude that the FeS_2 discs catalyst is indeed generating hydrogen gas.

3.4   Conclusions

Electrocatalytic measurement results show that the 2D disc structure had the best

30

efficiency compared to 1D and 3D FeS$_2$ structures with an onset potential near 0 vs RHE and overpotential close to that of Pt. The exchange current density for the 2D disc structures was calculated to be 2.2 μA cm^{-2} with a transfer coefficient of 0.71 which indicate high catalytic activity. Hydrogen generation was confirmed using an SECM technique and the discs were shown to be stable under reactive conditions for over 125 hours without severe degradation. Accounting for the extremely low-cost of the FeS$_2$ disc nanostructure with its excellent catalytic performance the 2D FeS$_2$ discs are a promising HER electrocatalyst.

3.5   Materials and Methods

All materials and methods in this section respectively were procured and generated by our collaborators K.C. Leonard and J. Barforoush.

3.5.1   Materials

Carbon black (Alfa-Aesar, acetylene, 100% compressed, ≥99.9%), monobasic dihydrate sodium phosphate (Acros Organics, ≥99%), and dibasic sodium phosphate (Acros Organics, anhydrous, ACS Reagent) were used as received.

3.5.2   Electrode Fabrication

A suspension was made by combining 5 mg carbon black, 200 μL of 5 wt% Nafion solution (Fuel Cell Earth), and 1 mL of ~50 mg/mL of either the FeS$_2$ wires or discs suspended in chloroform. Because of the difference in concentration between the wires/discs and the cubes, the FeS$_2$ cubes suspension was fabricated by combining 5 mg carbon black, 100 μL of 5 wt% Nafion solution, and 500 μL of ~12.5 mg/mL FeS$_2$ cubes suspended in chloroform. Each nanostructure suspension was sonicated for ~15 min then <10 μL was dropcasted on a 3 mm diameter glassy carbon electrode (CH Instruments) and allowed to dry for ~15 min before testing.

A laser capillary pipet puller (Model P-2000, Sutter Instruments, USA), quartz capillaries

(1 mm O.D., 0.3 mm I.D., 7.5 cm in length, Sutter Instruments, USA), 200 μm diameter Pt wire (Electron Microscopy Sciences 99.95% Pt wire), conductive silver epoxy (Circuit Works, USA), and silver connection wire (30 AWG, Belden, USA) were utilized in the fabrication of 200 μm SECM tip electrodes. MicroCloth polishing disks (Buehler, Canada), alumina micropolish (1 μm, 0.3 μm, Buehler, Canada), and MicroCut 1200 grit silicon carbide grinding paper (P2500, Buehler, Canada) were utilized to polish SECM tips before experiments.

Microdisk Pt electrodes 200 μm in diameter were fabricated for the SECM tip. The 200 μm Pt wire was centered in the quartz capillary before sealing the capillary to the wire and pulling to a tip with a laser capillary pipet puller (Sutter P-2000). Course polishing of the electrode tip with 1200 grit silicon carbide grinding paper was performed before fine polishing with 1 μm and 0.3 μm alumina micropolish, consecutively. Silver connection wire lightly coated with silver epoxy was inserted into the open end of the capillary tip electrode such that the silver epoxy was connecting the silver connection wire and the Pt wire. The SECM tip electrode was allowed to dry in a Model 30GC Lab Oven (Quincy Lab Inc.) at ~100 °C for ~20 min before using.

3.5.3 Electrochemical Characterization

Electrochemical measurements were performed in a glass cell with a simple 3-electrode configuration and carried out in a 0.1 M pH 7 phosphate buffer solution (PBS) bubbled with argon for ~5 min before use. The 0.1 M PBS was made by combining 4 mL of 1 M NaH_2PO_4 and 6 mL of 1 M Na_2HPO_4 and diluting with 90 mL of deionized Milli-Q water. The electrochemical measurements used either the FeS_2 coated 3 mm glassy carbon electrode, or a bare 3 mm glassy carbon electrode, or a bare 2 mm Pt electrode (CH Instruments) as the working electrode, a Pt wire (CH Instruments) as the counter electrode, and an Ag/AgCl electrode with porous Teflon tip (CH Instruments) as the reference electrode; however, the experiments were reported using the

reversible hydrogen electrode as the reference potential. Linear sweep voltammetry (LSV) experiments were performed at 1 mV s^{-1} with a CHI660E potentiostat (CH Instruments). All reported LSVs were corrected for double-layer capacitance and uncompensated resistance. The FeS$_2$ discs stability test was performed by utilizing chronoamperometry at an applied potential of -0.14 V vs RHE, with stirring provided by a magnetic stir bar to overcome mass transfer limitations. Time average data was recorded with each data point corresponding to an average current over 5 minutes.

3.5.4   SECM Characterization

The scanning electrochemical microscopy (SECM) experiments were performed in a Teflon cell using either the FeS$_2$ discs coated 3 mm glassy carbon electrode, or a bare 3 mm glassy carbon electrode, or a bare 2 mm Pt electrode as the substrate, a 200 μm Pt ultramicroelectrode (UME) as the SECM tip, a 200 μm Pt wire (Electron Microscopy Instruments) as the counter electrode, and an Ag/AgCl electrode with porous Teflon tip as the reference electrode with 0.1 M PBS, bubbled with argon for ~10 min, as the electrolyte. The SECM tip electrode was positioned approximately 100 μm away from the substrate electrode before scanning. Scanning was performed with the substrate electrode at a negative potential sufficient to produce hydrogen while the SECM tip electrode was held at a positive potential sufficient to collect hydrogen. A 666.67 μm/s scanning speed was utilized with 100 μm steps over a 3500 μm x 3500 μm area for the Pt substrate electrode, or a 4000 μm x 4000 μm area for the FeS$_2$ discs coated glassy carbon and bare glassy carbon substrate electrodes.

4   Conclusions and Future Work

Novel low-dimensional hyperthin FeS$_2$ nanostructures were generated by a scalable modified hot-injection technique. Low reaction temperatures kinetically confined the reaction to its early stages and prevented Ostwald ripening and oriented attachment from occurring to form

larger 3D structures. Also with these slower kinetics two separate nucleation and growth events were observed and increasing temperature caused a third to occur. Subsequent manipulation of the sulfur concentration in the initial reaction promoted one-dimensional or two-dimensional growth. To expand on this relationship of increasing sulfur concentration yielding increased dimensional growth more testing would need to be done to see if 3D structures could be achieved by using extreme sulfur concentrations. Furthermore, increased dwell times allowed for stoichiometric control of products to produce a 1:2 Fe:S structure but size limitations did not allow for definitive characterization. Additional structural characterization using X-ray photoelectron spectroscopy (XPS) may be necessary to confirm true elemental composition as well as composition of the different layers in the materials.

The electrocatalytic performance of these 1D and 2D FeS_2 materials as tested against platinum as well as a common 3D FeS_2 structure revealed the 2D structure's high relative efficiency. The near zero onset potential of the 2D structure was similar to platinum and possessed a low overpotential near 0 vs RHE.   Both had calculated charge transfer coefficients of 0.71 and the exchange current densities calculated using Butler-Volmer equations from best-fit lines yielded values of 2.2 and 8.0 $\mu A\ cm^{-2}$ for the 2D structures and platinum, respectively. Scanning electrochemical microscopy (SECM) confirmed the formation of hydrogen and subsequent stability test showed stable performance for over 125 hours at constant potential. To fully demonstrate the stability of these materials a long term cycling tests need to be performed as this would better mimic real-world conditions. Future work would also include SEM characterization of the electrodes before and after catalytic testing to ensure that the applied bias is not causing structural or morphological changes through repeated use or as a function of time.

Overall the fundamental reaction mechanism for producing 1D and 2D materials is now better understood and it has been demonstrated that these functional low-dimensional FeS_2

nanomaterials are promising precious metal electrocatalyst replacements.

5   References

1.   *Solar hydrogen generation toward a renewable energy future*. New York, NY : Springer: New York, NY, (2008).
2.   Steward, D., Ramsden, T., Harrison, K. Hydrogen for energy storage analysis overview: National Renewable Energy Laboratory; 2010.
3.   Turner, J.A. Sustainable Hydrogen Production. *Science*, **305,** 972-974 (2004).
4.   Srinivasan, S., Mosdale, R., Stevens, P., Yang, C. FUEL CELLS: Reaching the Era of Clean and Efficient Power Generation in the Twenty-First Century. *Annual Review of Energy and the Environment*, **24,** 281-328 (1999).
5.   Mckone, J.R.*, et al.* Earth-abundant hydrogen evolution electrocatalysts. *Chemical Science*, **5,** 865-878 (2014).
6.   Ennaoui, A.*, et al.* Iron disulfide for solar energy conversion. *Solar Energy Materials and Solar Cells*, **29,** 289-370 (1993).
7.   Murray, C.B., Kagan, C.R., Bawendi, M.G. Synthesis and characterization of monodisperse nanocrystals and close-packed nanocrystal assemblies. *Annual Review of Materials Science*, **30,** 545-610 (2000).
8.   Lamer, V.K., Dinegar, R.H. Theory, Production and Mechanism of Formation of Monodispersed Hydrosols. *J. Am. Chem. Soc.*, **72,** 4847-4854 (1950).
9.   Gong, M., Kirkeminde, A., Ren, S. Symmetry-Defying Iron Pyrite (FeS2) Nanocrystals through Oriented Attachment. *Sci. Rep.*, **3,** (2013).
10.   Wadia, C., Alivisatos, A.P., Kammen, D.M. Materials availability expands the opportunity for large-scale photovoltaics deployment. *Environ. Sci. Technol.*, **43,** 2072-2077 (2009).
11.   *U.S. Geological Survey: Mineral Commodity Summaries 2012*, (2012).
12.   Macpherson, H.A., Stoldt, C.R. Iron pyrite nanocubes: Size and shape considerations for photovoltaic application. *ACS Nano*, **6,** 8940-8949 (2012).
13.   Bai, Y.*, et al.* Universal synthesis of single-phase pyrite FeS_2 nanoparticles, nanowires, and nanosheets. *J. Phys. Chem. C*, **117,** 2567-2573 (2013).
14.   Kirkeminde, A.*, et al.* Synthesis and optoelectronic properties of two-dimensional FeS_2 nanoplates. *ACS Appl. Mater. Interfaces*, **4,** 1174-1177 (2012).
15.   Kirkeminde, A.*, et al.* Iron sulfide ink for the growth of pyrite crystals. *Nanotechnology*, **25,** 205603 (2014).
16.   Bi, Y.*, et al. Nano Lett.*, **11,** 4953 (2011).
17.   A. Ennaoui*, et al.* Photoelectrochemical energy conversion obtained with ultrathin organo-metallic-chemical-vapor-deposition layer of FeS_2 (pyrite) on TiO_2. *J. Electrochem. Soc.*, **139,** 2514-2518 (1992).
18.   Chatzitheodorou, G.*, et al.* Thin photoactive FeS_2 (pyrite) films. *Mater. Res. Bull.*, **21,** 1481-1487 (1986).
19.   Aricò, A.S.*, et al.* Electrodeposition and characterization of iron sulphide thin films. *Mater. Lett.*, **13,** 12-17 (1992).
20.   Vogt, H., Chattopadhyay, T., Stolz, H.J. Complete first-order Raman spectra of the pyrite structure compounds FeS_2, MnS_2 and SiP_2. *J. Phys. Chem. Solids*, **44,** 869-873 (1983).
21.   Lutz, H.D., Müller, B. Lattice vibration spectra. LXVIII. Single-crystal Raman spectra of marcasite-type iron chalcogenides and pnictides, FeX_2 (X=S, Se, Te; P, As, Sb). *Phys. Chem. Miner.*, **18,** 265-268 (1991).
22.   Yang, J., Shin, H.S. Recent advances in layered transition metal dichalcogenides for hydrogen evolution reaction. *J. Mater. Chem. A*, **2,** 5979-5985 (2014).

23. Kong, D.S.*, et al.* First-row transition metal dichalcogenide catalysts for hydrogen evolution reaction. *Energy Environ. Sci.*, **6,** 3553-3558 (2013).
24. Faber, M.S., Jin, S. Earth-abundant inorganic electrocatalysts and their nanostructures for energy conversion applications. *Energy Environ. Sci.*, **7,** 3519-3542 (2014).
25. Wu, Z.Z.*, et al.* WS_2 nanosheets as a highly efficient electrocatalyst for hydrogen evolution reaction. *Appl. Catal., B*, **125,** 59-66 (2012).
26. Faber, M.S.*, et al.* Earth-abundant metal pyrites (FeS_2, CoS_2, NiS_2, and their alloys) for highly efficient hydrogen evolution and polysulfide reduction electrocatalysis. *J. Phys. Chem. C*, **118,** 21347-21356 (2014).
27. Jaramillo, T.F.*, et al.* Identification of active edge sites for electrochemical H_2 evolution from MoS_2 nanocatalysts. *Science*, **317,** 100-102 (2007).
28. Li, Y.G.*, et al.* MoS_2 nanoparticles grown on graphene: An advanced catalyst for the hydrogen evolution reaction. *J. Am. Chem. Soc.*, **133,** 7296-7299 (2011).
29. Lukowski, M.A.*, et al.* Enhanced hydrogen evolution catalysis from chemically exfoliated metallic MoS_2 nanosheets. *J. Am. Chem. Soc.*, **135,** 10274-10277 (2013).
30. Bard, A., Faulkner, L. *Electrochemical Methods: Fundamentals and Applications*. John Wiley & Sons, Inc, (2001).
31. Leonard, K.C., Bard, A.J. The study of multireactional electrochemical interfaces via a tip generation/substrate collection mode of scanning electrochemical microscopy: the hydrogen evolution reaction for Mn in acidic solution. *J. Am. Chem. Soc.*, **135,** 15890-15896 (2013).
32. Bard, A.J.*, et al.* Chemical imaging of surfaces with the scanning electrochemical microscope. *Science*, **254,** 68-74 (1991).
33. Wei, C., Bard, A.J., Mirkin, M.V. Scanning Electrochemical Microscopy .31. Application of SECM to the study of charge-transfer processes at the liquid-liquid interface. *J. Phys. Chem.*, **99,** 16033-16042 (1995).
34. Sun, T., Yu, Y., Zacher, B.J., Mirkin, M.V. Scanning Electrochemical Microscopy of Individual Catalytic Nanoparticles. *Angew. Chem.*, **53,** 14120-14123 (2014).